



Radiation-induced segregation in desensitized type 304 austenitic stainless steel

Parag Ahmedabadi^{a,*}, V. Kain^a, K. Arora^b, I. Samajdar^c, S.C. Sharma^d, P. Bhagwat^d

^a Materials Science Division, Bhabha Atomic Research Centre, Trombay, Mumbai 400 085, India

^b PEC University of Technology, Chandigarh, India

^c Department of Metallurgical Engineering and Materials Science, Indian Institute Technology Bombay, Powai, Mumbai 400 076, India

^d Nuclear Physics Division, Bhabha Atomic Research Centre, Trombay, Mumbai 400 085, India

ARTICLE INFO

Article history:

Received 27 December 2010

Accepted 17 June 2011

Available online 7 July 2011

Keywords:

Austenitic stainless steel
Desensitization
Proton-irradiation
Electrochemical potentiokinetic reactivation
Atomic force microscopy
Radiation-induced segregation

ABSTRACT

Radiation-induced segregation (RIS) in desensitized type 304 stainless steel (SS) was investigated using a combination of electrochemical potentiokinetic reactivation (EPR) test and atomic force microscopy (AFM). Desensitized type 304 SS was irradiated to 0.43 dpa (displacement per atom) using 4.8 MeV protons at 300 °C. The maximum attack in the EPR test for the irradiated desensitized SS was measured at a depth of 70 μm from the surface. Grain boundaries and twin boundaries got attacked and pit-like features within the grains were observed after the EPR test at the depth of 70 μm. The depth of attack, as measured by AFM, was higher at grain boundaries and pit-like features as compared to twin boundaries. It has been shown that the chromium depletion due to RIS takes place at the carbide–matrix as well as at the carbide–carbide interfaces at grain boundaries. The width of attack at grain boundaries after the EPR test of the irradiated desensitized specimen appeared larger due to the dislodgement of carbides at grain boundaries.

© 2011 Elsevier B.V. All rights reserved.

1. Introduction

Radiation-induced segregation (RIS) is non-equilibrium segregation of alloying elements caused by generation and diffusion of point defects [1–4]. The RIS is typically observed for in-core components in light water reactors (LWR). The RIS is considered to be part of a complex process that increases the susceptibility to irradiation assisted stress corrosion cracking (IASCC) of austenitic stainless steel (SS) in LWR [1–5]. RIS leads to depletion of chromium at grain boundaries, without formation of chromium rich carbides in contrast to chromium rich carbide formation leading to chromium depletion in the case of thermally sensitized material [6].

The studies to relate the effects of neutron irradiation on intergranular stress corrosion cracking (IGSCC) of thermally sensitized SS have shown [7–9] an increase in susceptibility to IGSCC with neutron fluences up to 1.1×10^{24} n/m² ($E \geq 1$ MeV). Studies [10–12] have also indicated that prior thermal sensitization increased the susceptibility to IGSCC in irradiated austenitic stainless steel. For example, in sensitized type 304 SS, equivalent amount of chromium depletion was attained for a neutron fluence of 1.0×10^{24} n/m² as compared to 1×10^{26} n/m² for the non-sensitized material [10]. The effect of sensitization on RIS has been studied extensively [11–13] and is shown to result in narrower chromium depletion zones [11] and nickel enrichment under Helium-ion damage [12].

It has been shown [13] that the chromium-concentration profile gets narrower and deeper upon proton-irradiation. It was argued that [13] during irradiation, concentration flux and the inverse Kirkendall flux compete with each other and Cr will be further depleted at grain boundaries if the inverse Kirkendall flux is greater than the concentration flux. The Cr profile would be narrower if the concentration flux is greater than the inverse Kirkendall flux.

Though there are many studies [7–13] showing enhanced RIS in sensitized austenitic stainless steels, the effects of desensitization on the RIS behavior have not been investigated. It may be noted that desensitization in austenitic stainless steels leads to formation of $M_{23}C_6$ ($M = Cr, Fe$) hence to an indirect enrichment of Cr at grain boundaries without any chromium depletion zones adjacent to grain boundaries. Such an indirect enrichment of Cr at grain boundaries may help in reducing the extent of RIS (particularly Cr depletion) at grain boundaries. As RIS is a part of the complex process that leads to irradiation assisted stress corrosion cracking (IASCC), improvement in resistance to RIS may also improve the resistance to IASCC. In this study, effect of desensitization on the nature and extent of RIS in type 304 SS was investigated using 4.8 MeV proton-irradiation at 300 °C. A combination of double loop electrochemical potentiokinetic reactivation (DL-EPR) test and atomic force microscopy (AFM) was used to characterize the extent of RIS and to link the RIS behavior with different microstructural features. The EPR method was used in the past to characterize RIS in austenitic SS [14–19]. AFM examination was done to evaluate the depth of attack on various microstructural features after the

* Corresponding author. Tel.: +91 22 25595402; fax: +91 22 25505151.

E-mail address: adit@barc.gov.in (P. Ahmedabadi).

DL-EPR test for the irradiated specimen. It may be noted that characterization of RIS by analytical techniques (such as scanning transmission electron microscopy–energy dispersive spectroscopy: STEM–EDS and Auger electron spectroscopy: AES) reveal information about irradiation induced microstructural and microchemical changes and electrochemical techniques yield information about the influence of irradiation induced microstructural and microchemical changes on the corrosion characteristics of the material [16].

2. Material and experimental

2.1. Materials and heat-treatment

The material chosen for the present investigation was obtained in the form of a 3 mm thick plate. The chemical composition (in wt.%) of this alloy is C: 0.054, Cr: 19.97, Ni: 7.97, Si: 0.59, Mn: 1.85, P: 0.035 and S: 0.006. The desensitization was carried out on the as-received material at 750 °C for 360 h [20]. The desensitization heat treatment results in grain boundaries saturated with chromium-rich $M_{23}C_6$ carbides and no chromium depleted regions adjacent to grain boundaries. To check the sensitization behavior of the as-received material, a specimen was subjected to a sensitization heat-treatment at 675 °C for 1 h. A smaller sample was cut from the plate and was polished metallographically followed by electro-polishing before proton irradiation. An electrolyte of 90% methanol and 10% perchloric acid solution was used at a temperature of –30 °C and at 20 V dc for electro-polishing.

2.2. Proton-irradiation

Proton irradiation was performed using a specifically designed assembly at PELLETRON accelerator, a joint Bhabha Atomic Research Centre–Tata Institute of Fundamental Research (BARC–TIFR) facility. Proton-irradiation was carried out using a 4.8 MeV proton beam at a dose rate of 1.4×10^{-6} dpa/s (displacement per atom/s). The irradiated surface area was approximately 7 mm². The specimen temperature was maintained during irradiation at 300 ± 5 °C and the level of vacuum was at 1.3×10^{-5} N/m². The proton-irradiated specimen was allowed to cool down for a period of a month before doing further analysis to remove any residual radioactivity. The average current during proton-irradiation was approximately 500 nA and the specimen was irradiated to 0.43 dpa. The experimental doses and dose rates were calculated using SRIM2003 software [21], while accumulated irradiation damage due to proton-irradiation, in terms of dpa, was estimated using NRT equation [22],

$$\text{dpa} = \frac{0.8}{2E_d} \left(\frac{dE}{dx} \right)_n \frac{\phi_t}{\rho} \quad (1)$$

where E_d is the displacement energy, $(dE/dx)_n$ is the linear energy transfer (LET) per ion to target by nuclear processes, ϕ_t is the fluence per unit area and ρ is the atomic density. $(dE/dx)_n$ and was obtained from SRIM by summing up phonon and binding energy profiles. The binding energy profile was obtained by vacancy profile multiplied by binding energy (3 eV). The damage profile obtained using SRIM for proton-irradiation was given a curve-fitting using the following equation (4-parameter Pseudo-Voigt equation):

$$y = a \left[c \left(\frac{1}{1 + \alpha^2} \right) + (1 - c) \exp(-0.5\alpha^2) \right], \quad (2)$$

where $\alpha = (x - x_0)/b$ and a , b , c , x_0 are constants, x is depth (in micron) and y is the damage corresponding to given x .

2.3. Electrochemical potentiokinetic reactivation (EPR) test

The extent of chromium depletion in un-irradiated as received, sensitized, and desensitized as well as the irradiated desensitized SS specimens was evaluated using the DL-EPR test. The DL-EPR test was carried out [23] in a solution of 0.5 mol/l H_2SO_4 and 0.01 mol/l KSCN (de-aerated) at room temperature. The potential was scanned from –30 mV vs. open circuit potential (OCP) to +300 mV_{SCE} (mV vs. saturated calomel electrode) and then back to OCP at a scan rate of 6 V/h. The non-irradiated area on each specimen was masked with a lacquer and only the irradiated area was exposed to the solution. The result of the DL-EPR test is reported as DL-EPR value which is the ratio of the maximum current in the backward loop to that in the forward loop, multiplied by 100. The maximum damage due to proton irradiation to occur at 70 μm [21] below the surface for 4.8 MeV protons. Therefore, starting from the as-irradiated surface, the DL-EPR test was repeated after removing the affected-layer after each test, until the un-irradiated/un-affected material was reached. The thickness of the specimen after each DL-EPR test was measured using a micrometer screw with a least count of 1 μm. After each DL-EPR test, the affected layer was removed by grinding using fine emery-papers followed by polishing using 0.5 μm diamond paste.

2.4. AFM examination

After each DL-EPR test, the specimen was examined using NT-MDT Solver Pro scanning probe microscope in semi-contact mode. The extent of attack caused by the DL-EPR test was measured as depth of attack on various microstructural features like grain boundaries, twin boundaries, and any other feature within the grains.

3. Results

3.1. Characterization of the un-irradiated material

The hardness of the as-received material was 205 HV (Vickers hardness), higher than that of a typical solution-annealed type 304 SS (i.e. 170 HV). The grain size of the as-received material was 18 μm, corresponding to an ASTM grain size number 9. After the desensitization heat treatment, the hardness reduced to 180 HV with no change in grain size. The respective DL-EPR values for the as-received, sensitized and desensitized samples were 0.07, 3.89 and 0.06. Optical micrographs after DL-EPR test and the DL-EPR curves for the as-received, sensitized and desensitized samples are shown in Fig. 1. Optical micrographs (Fig. 1a and c) for the as-received and the desensitized specimen did not show significant attack on the grain boundaries, while the same for the sensitized sample demonstrated severe attack on almost all the grain boundaries, as depicted in Fig. 1b. The DL-EPR curves for the as-received sensitized and desensitized specimens are shown in Fig. 1d, indicating a higher current during the reactivation loop for the sensitized specimen. On the other hand, a very low current during the reactivation loop for the desensitized sample indicated the effectiveness of the desensitization heat-treatment in removing chromium depletion (with chromium below 12 wt.% [20]) regions adjacent to grain boundaries.

3.2. Electrochemical characterization of the irradiated specimen

Fig. 2 shows the damage profiles calculated using Eq. (1) and the variation of DL-EPR values with depth. The typical profile consisted of a uniform damage region for the first 70 μm of depth, followed by the peak damage region between 70 and 80 μm. The variation of

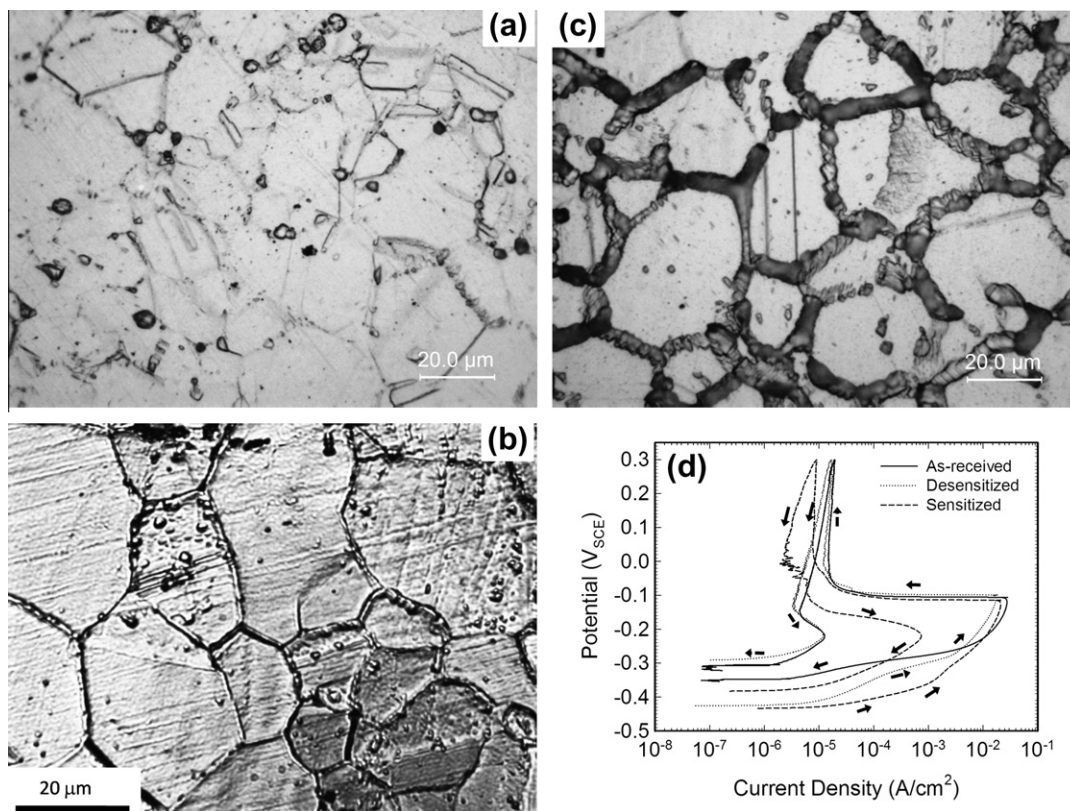


Fig. 1. Micrographs after the DL-EPR test for the (a) as-received (DL-EPR value: 0.07) (b) sensitized at 675 °C for 1 h (DL-EPR value: 3.89) and (c) desensitized (DL-EPR value: 0.06) specimens. (d) The DL-EPR curves for the un-irradiated as-received, sensitized and desensitized specimens, the un-irradiated sensitized specimen shows the highest current density in the reverse loop.

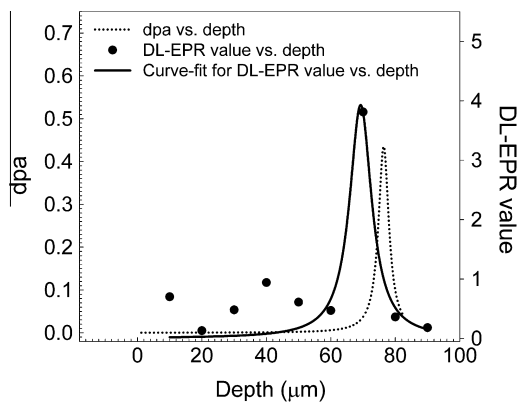


Fig. 2. Proton-irradiation damage vs. depth in the irradiated (0.43 dpa) desensitized sample. The figure shows SRIM [18] estimated trend, DL-EPR measurement points and trend-fitting (using Eq. (2)) for the DL-EPR data points. The trend in DL-EPR vs. depth profile was very similar to that in damage vs. depth profile, predicted by SRIM.

DL-EPR values with the depth is also plotted in the same graph and DL-EPR values were given a curve-fit using Eq. (2). The values of a , b , c and x_0 as defined in Eq. (2) are 3.9828 (2.6), 4.4898 (7.82), 1.00 (4.12) and 69.03 (4.68), respectively. The values in the brackets indicate standard deviation in estimation of the constants a , b , c and x_0 defined in Eq. (2). As shown in Fig. 2, the SRIM and the DL-EPR profiles were remarkably similar. The average DL-EPR value in the region of uniform damage was 0.54 (corresponding SRIM calculation was 0.031 dpa) and the maximum DL-EPR value was 3.81 (corresponding SRIM calculation was 0.43 dpa).

Table 1

The variation in current density (during the reactivation and the activation loop), the Flade potential, and the corresponding DL-EPR values at different depths for the desensitized specimen irradiated to 0.43 dpa.

Depth (μm)	I_r (μA/cm ²)	I_a (mA/cm ²)	DL-EPR value	Flade potential (mV _{SCE})
0	163.2	16.15	1.01	-76
10	199.0	28.43	0.70	-75
20	34.5	26.54	0.13	-76
30	144.0	30.0	0.47	-77
40	228.0	24.26	0.94	-40
50	142.0	23.28	0.61	-63
60	135.0	28.72	0.47	-57
70	733.0	19.24	3.81	+15
80	89.8	24.94	0.36	-25
90	59.0	32.78	0.18	-52

The Flade potential is the potential at which the depassivation starts on the surface of the material. For the case of austenitic stainless steels, it is taken as the start of the reactivation loop during the EPR test. The Flade potentials for different depths for the desensitized specimen irradiated to 0.43 dpa are given in Table 1 along with current values in activation and reactivation loops. The Flade potential for the irradiated desensitized specimen was in the range of -77 to +15 mV_{SCE} and the highest value was noticed at the depth of 70 μm with maximum DL-EPR value of 3.81. The Flade potentials values for the as-received and the desensitized specimens (in un-irradiated condition) were -170 and -150 mV_{SCE}, respectively, as shown in the Fig. 1d. Thus, the Flade potentials for the irradiated surfaces were considerably higher than that for the as-received and un-irradiated desensitized specimen. The

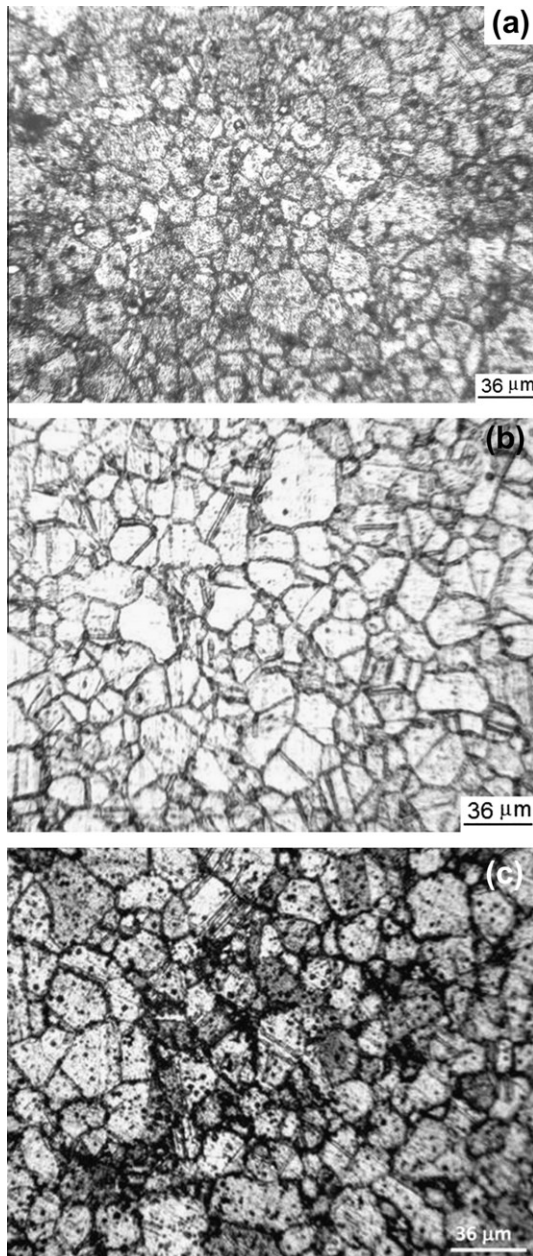


Fig. 3. Optical micrographs after the DL-EPR test of the irradiated (0.43 dpa) desensitized sample at: (a) as-irradiated surface (DL-EPR value: 1.05), showing severe attack at grain boundaries and within grains, (b) a depth of 40 μm (DL-EPR value: 0.47), showing attacked grain boundaries and negligible pit-like features within grains, and (c) a depth of 70 μm (DL-EPR value: 3.81) showing severe attack on grain boundaries and pit-like features within grains.

Flade potential for the sensitized (675 $^{\circ}\text{C}$ for 1 h) material was also higher ($-50 \text{ mV}_{\text{SCE}}$) than that of the as-received specimen.

3.3. Optical microscopic examination

Fig. 3 collates optical micrographs after the respective DL-EPR tests at different depths for the irradiated desensitized SS. As shown in **Fig. 3a**, the as-irradiated surface shows severe damage within grains as well as at grain boundaries. This is because the free surface acts as a large defect sink for point defects generated during irradiation leading to severe damage. **Fig. 3b** shows the micrograph at the depth of 40 μm (DL-EPR value: 0.37), showing attack on grain boundaries. **Fig. 3c** depicts the micrograph at the depth of 70 μm where the maximum damage was noticed with DL-EPR value of 3.81. The attack was noticed on many grain boundaries along with many pit-like features inside the grain matrix. It may be noted that the number of pit-like features within grains was less at the depth of 40 μm than that at the depth of 70 μm .

3.4. AFM examination

Fig. 4 shows the AFM images at different depths after the DL-EPR test for the desensitized specimen irradiated to 0.43 dpa. It illustrates attack on different microstructural features such as regions adjacent to grain boundary carbides at the depth of 30 μm (**Fig. 4a**), a grain boundary at the depth of 70 μm (**Fig. 4b**), twin boundaries at the depth of 70 μm (**Fig. 4c**), and a pit-like feature within grain at the depth of 70 μm (**Fig. 4d**). The variations in the depth of attack on different microstructural features viz. grain boundaries, twin boundaries and pit-like features are depicted in **Fig. 5** for three different depths. As shown in the figure, the depth of attack was higher on grain boundaries and pit-like features in comparison to the depth of attack on twin boundaries. The depth of attack was as high as 1.2 μm on grain boundaries as shown in **Fig. 5a**.

The depths of attack on various microstructural features are also summarized in **Table 2** with average values for different depths. It is apparent that the depth of attack on various microstructural features increased with increase in DL-EPR values: increased depth of attack on twin boundaries (~ 1.4 times), pit-like features within grains (~ 1.8 times), and grain boundaries (~ 2.2 times) was observed. **Fig. 6** shows the variation of the average depth of attack for different microstructural features with DL-EPR values, along with linear-regression. As can be seen from the slopes of linear-fit, the increase in the depth of attack with DL-EPR value was more for grain boundaries and pit-like features within grains as compared to that for twin boundaries. In terms of the relative depth of attack the various microstructural features can be represented in increasing order as twin-boundary > pit-like features > grain boundaries. For comparison, the depth of attack on grain boundaries after DL-EPR in the sensitized (675 $^{\circ}\text{C}$ for 1 h, DL-EPR value 3.89) specimen was also measured using AFM. **Fig. 7** depicts an AFM micrograph of the sensitized specimen at a grain boundary, the depth of attack at the given location was 1.6 μm and the width of attack was around 4 μm . Thus, the width and depth of attack for thermally sensitized specimen was much higher than that in the desensitized specimen irradiated to 0.43 dpa. The

Table 2

The depth of attack (as measured by AFM) on various microstructural features after the DL-EPR test at different depths. The table provides the range of attack as well as the average values (in brackets).

Depth from the top surface (μm)	Depth of attack (nm) (Grain boundary)	Depth of attack (nm) (Twin boundary)	Depth of attack (nm) (Pit-like features within grains)
40	350–400 (374)	325–450 (414)	475–600 (505)
70	700–1200 (900)	450–650 (547)	700–1000 (850)
90	350–475 (364)	400–600 (438)	350–420 (387)

typical width of attack at the depth of 70 μm (maximum DL-EPR value 3.81) for the desensitized specimen irradiated to 0.43 dpa was approximately 1 μm . This is in line with the reported results [16,17] indicating that the chromium depletion developed due to RIS is much narrower compared to that developed by thermal sensitization.

Fig. 8 schematically summarizes experimental results obtained in the present investigation, indicating attack on grain boundaries, twin boundaries and pit-like features within grains for the desensitized specimen irradiated to 0.43 dpa while the attack is confined to grain boundaries for the un-irradiated as-received, sensitized and the desensitized SS after the DL-EPR test. As observed in the irradiated desensitized specimen, the un-irradiated sensitized specimen also showed attack on almost all grain boundaries. However, the attack on twin boundaries and pit-like features was not noticed for the un-irradiated sensitized specimen. Thus, for the irradiated desensitized specimen, the attack on grain boundaries, twin-boundaries and pit-like features contributed to the anodic current during the reverse loop of DL-EPR whereas for the sensitized specimen, attack only on grain boundaries contributed to the anodic current.

4. Discussion

4.1. Electrochemical characterization of the irradiated specimen

The DL-EPR values (for different depths) for the irradiated desensitized specimen were higher than that for the as-received and un-irradiated desensitized material indicating the presence of chromium depletion (due to RIS) regions in the irradiated desensitized specimen. The maximum DL-EPR value (3.81) for the irradiated specimen was of the similar order to that of the sensitized (heat-treated at 675 $^{\circ}\text{C}$ for 1 h) specimen (DL-EPR value: 3.89). That indicates the comparable levels of chromium depletion in the irradiated desensitized specimen at the depth of maximum attack and the sensitized specimen.

The increased values of the Flade potentials for the irradiated specimen imply the presence of weak passive films on the irradiated specimen. The Flade potential is a measure of the inherent stability of the passive film for stainless steel, higher the Flade potentials weaker the passive films [16]. This could be either due to chromium depletion or due to the higher diffusivities of cation vacancies in the film and/or the metal substrate due to dislocations as suggested by the studies on characteristic of passive films in stainless steels [24,25]. The Flade potentials of the irradiated specimen were higher (-50 to -77 mV_{SCE}) even for the lower DL-EPR values in the range of 0.13–0.94 compared to those for the un-irradiated SS. This could be due to a weaker passive film because of a higher concentration of point defects generated due to irradiation. As explained earlier, the higher concentration of point defects would increase diffusivities of cation vacancies in the passive film; leading to more dissolution. This also suggests that even for the low levels of chromium depletion, as indicated by lower DL-EPR values for the depths between 20 and 60 μm , the passive film over the irradiated austenitic stainless steel surface was weaker due to the presence of point defects. The value of the Flade potential was the highest for the maximum DL-EPR value; implying that the increase in DL-EPR values was accompanied by increase in the value of the Flade potential.

4.2. Microscopic examination

The irradiated specimen showed attacked regions (after the DL-EPR test) within the matrix (pit-like features) and near grain boundaries indicating chromium depletion (due to RIS) regions at

these locations. Pit-like features within the matrix were reported earlier in irradiated austenitic stainless steels after the EPR test [16,17]. Previous studies had revealed that chromium depletion can occur within grains at dislocation loops [26,27] formed during irradiation. Such chromium depleted regions within grains would get attacked during DL-EPR and appear as pit-like features.

As illustrated in Fig. 5, AFM measurements after the DL-EPR test (on the desensitized specimen irradiated to 0.43 dpa) had indicated that the attack on grain boundaries and pit-like features within the grains was more as compared to that at the twin-boundaries. The DL-EPR test attacks chromium depletion regions, indicating that the extent of chromium depletion (due to inverse Kirkendall effect) near grain boundaries and pit-like features were higher vis-à-vis that at the twin boundaries. Twin boundaries are essentially low-energy boundaries as compared random boundaries. It implies that the free energy available for adsorption of point-defects was higher at the carbide–matrix interface, the carbide–carbide interface and at the dislocation domain structure within grains as compared to that at the twin-boundaries. This was confirmed by the average depths of attack for grain boundaries, twin boundaries, and pit-like features for different depths as depicted in Fig. 6.

The increase in DL-EPR value was also accompanied with the increase in the depth of attack on various microstructural features like grain boundaries and pit-like features. It implies that increase in chromium depletion levels (as indicated by higher DL-EPR values) had increased the depth of attack on microstructural features during the DL-EPR test for the irradiated specimen.

4.3. Carbides at grain boundaries and RIS

It is known that unlike ASTM A 262 Practice A [28], the EPR test attacks only the chromium depletion regions (during the reverse loop) and not the M_{23}C_6 carbide [29]. In the present investigation it was observed that M_{23}C_6 carbide remained intact and the attack during the DL-EPR test had occurred adjacent to grain boundaries for lower DL-EPR values, as shown in Fig. 4a. However, M_{23}C_6 carbides were not noticed at peak damage with DL-EPR value of 3.81, as depicted in Fig. 4b. The attack on regions adjacent to grain boundaries for lower DL-EPR values and the removal of M_{23}C_6 carbide for the maximum DL-EPR value can be explained as follows.

Sensitization results in precipitation of M_{23}C_6 at grain boundaries and chromium depletion adjacent to grain boundaries. The desensitization treatment erases chromium depletion regions adjacent to grain boundaries whereas M_{23}C_6 at grain boundaries remains intact [20]. The sensitization process is dictated by a balance of carbon, nickel and chromium levels in stainless steels [30–34]. At the onset of sensitization, M_{23}C_6 carbides nucleate at grain boundaries and grow with time. The growth of M_{23}C_6 continues until the free carbon (the amount of carbon in excess of the solubility limit) in the matrix gets consumed. At this point, the chromium levels in chromium depleted zones (adjacent to grain boundaries) begin to increase by replenishment from the grain matrix.

The nucleation of carbide occurs simultaneously at various locations on a grain boundary and the growth of carbide nuclei occurs along grain boundaries as well as into the matrix. The nucleation and growth of M_{23}C_6 at grain boundaries thus creates two interfaces: one interface exists between the carbide and the matrix and another interface exists between two adjacent carbide particles.

The carbide particles (M_{23}C_6) on grain boundaries are incoherent in nature and have higher interfacial energy [35] due to larger size which is in the range of 50–100 nm. Also, due to the fact that a given carbide particle grows in two adjacent grains (with different

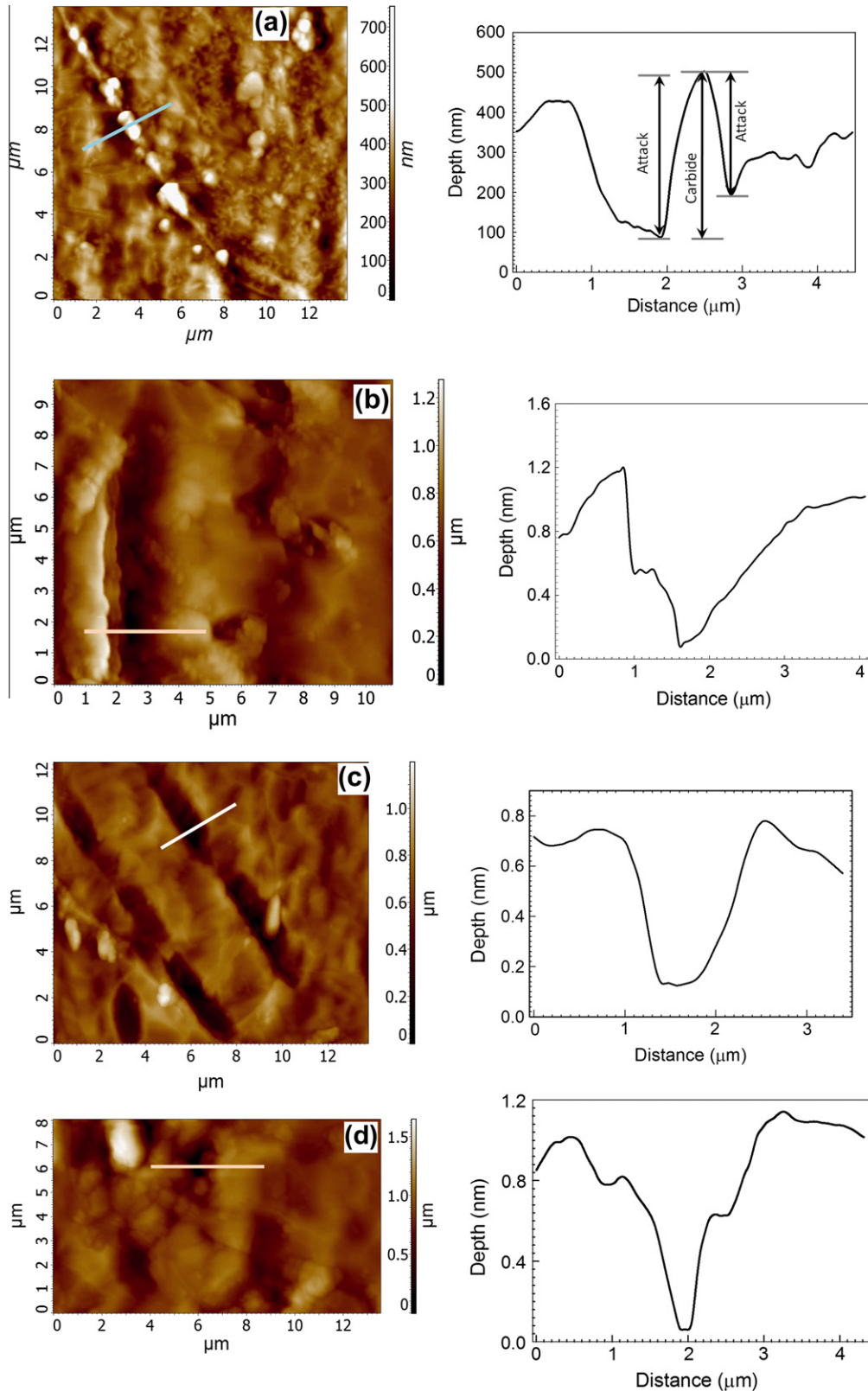


Fig. 4. AFM micrographs after the DL-EPR test for the desensitized specimen irradiated to 0.43 dpa illustrating attacks at (a) 30 μm depth (DL-EPR: 0.47) showing attack on regions adjacent to carbides at grain boundaries (b) 70 μm depth (DL-EPR: 3.81), showing attack on a grain boundary and dislodgement of carbides, the depth of attack is 1200 nm (c) 70 μm depth (DL-EPR: 3.81), showing attack on a twin boundary, the depth of attack is 600 nm and (d) 70 μm depth (DL-EPR: 3.81), showing attack on a pit-like feature within grains with depth of attack 900 nm.

crystallographic orientations), this introduces incoherency at the interface leading to higher interfacial free energy. Therefore, the

carbide–matrix and the carbide–carbide interfaces can act as defect sinks.

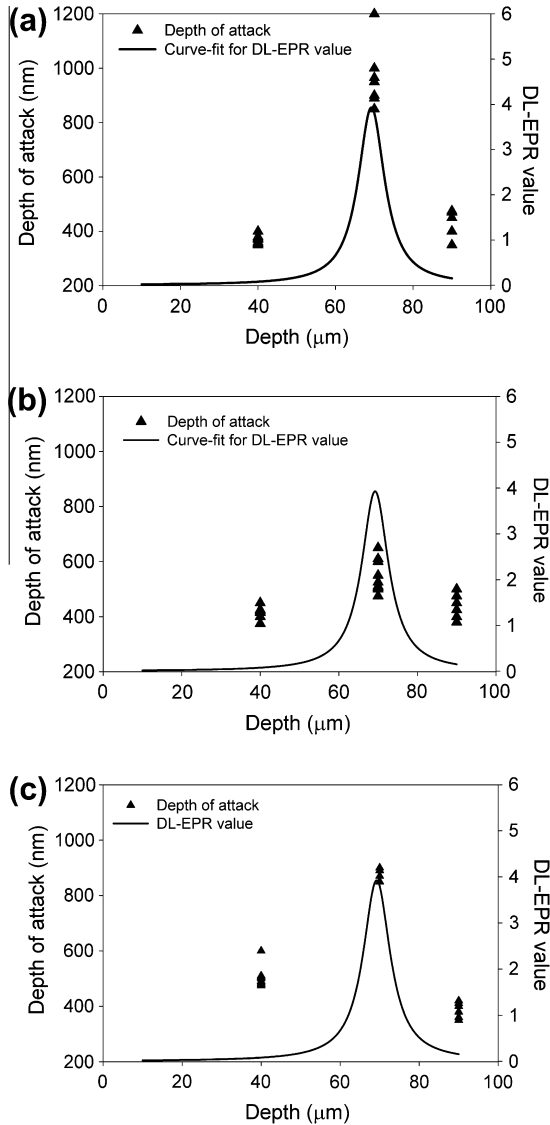


Fig. 5. The depth of attack, after the DL-EPR test on irradiated (0.43 dpa) desensitized specimen, at (a) grain boundaries (b) twin boundaries and (c) pit-like features within grains. Also included are the DL-EPR value vs. depth and the fitted (Eq. (2)) curve. The depth of attack was higher at grain boundaries and pit-like features within grains as compared to twin boundaries.

During irradiation at high temperature, point defects move to grain boundaries because of inverse Kirkendall effect and interstitial association binding mechanism [36,37]. In the case of grain boundaries saturated with carbides, migrating point defects first encounter the carbide–matrix interface and get adsorbed at the interface. Point defects adsorption can also occur at carbide–carbide interface. Thus, chromium depletion would first occur at the carbide–matrix interface because of adsorption of vacancies. This explains the observed results that the attack during the DL-EPR test in the uniform damage region first occurred adjacent to grain boundaries (Fig. 4a). As irradiation progresses, more point defects, particularly vacancies, migrate towards grain boundaries and adsorption of vacancies would then occur at the carbide–carbide interface in addition to the carbide–matrix interface. This is schematically represented as in Fig. 9. The attacked chromium depletion zones are shown black and carbides are shown in gray color. It illustrates the attack on regions adjacent to $M_{23}C_6$ carbide. In view of the three dimensional nature of carbide–matrix and carbide–carbide interfaces, at peak damage depth chromium

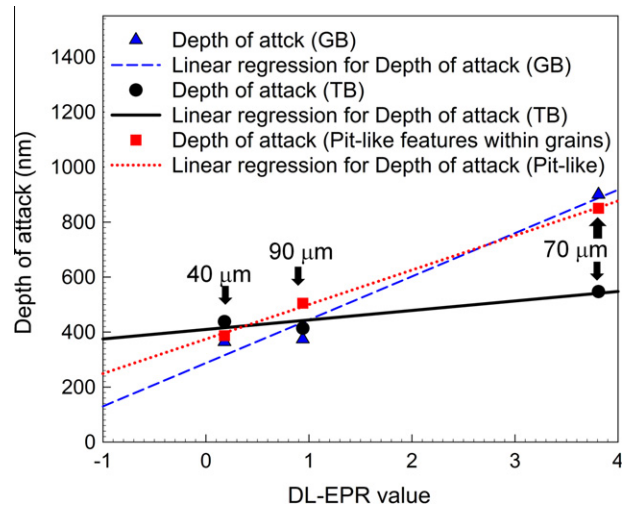


Fig. 6. The variation in the average depth of attack with the DL-EPR values for different depths for various microstructural features for the desensitized specimen irradiated to 0.43 dpa. The linear regression is also plotted for the each plot. The figure shows that increase in DL-EPR values showed more increase in the depth of attack for grain boundaries and pit-like features as compared to twin boundaries.

depletion zones would surround the entire carbide–carbide interface. Hence, the attack during DL-EPR selectively occurs at the carbide–matrix and the carbide–carbide interface and finally results in the removal/dislodgement of the carbide particles. Though the carbides themselves are not attacked during the EPR test [29]. A similar effect of oversized solute elements (cerium) acting as a site for precipitation of carbides during sensitization and for accommodation of the diffusing chromium atoms during low temperature sensitization in austenitic stainless was shown in a previously reported study [38].

4.4. Contribution of various microstructural features to anodic current

The total anodic current during the reactivation loop of the DL-EPR test is the sum of current emanating from various microstructural features like grain boundaries, twin boundaries, and pit-like features. Thus, the total current during the reactivation loop, I , is,

$$I = I_{GB} + I_{TB} + I_{Pit}$$

$$i \times A = (i_{GB} \times A_{GB}) + (i_{TB} \times A_{TB}) + (i_{Pit} \times A_{Pit})$$

$$i = \left(i_{GB} \times \frac{A_{GB}}{A} \right) + \left(i_{TB} \times \frac{A_{TB}}{A} \right) + \left(i_{Pit} \times \frac{A_{Pit}}{A} \right) \quad (3)$$

where I 's and i 's are total current and current density, respectively from microstructural features like grain boundaries (GB), twin boundaries (TB) and pit-like features (Pit). A is the total area of the specimen. The terms A , A_{GB} , A_{TB} and A_{Pit} are the total area, grain boundary area, twin boundary area, and pit-area, respectively.

The contribution to the total anodic current (from a given microstructural feature, f) is a function of the current (i_f) and the area fraction (A_f/A) of that particular microstructural feature. The current from a given microstructural feature during EPR testing is representative of the level of chromium depletion (due to RIS) in that microstructural feature. This level of chromium depletion on a given microstructural is directly related to the defect sink strength. The higher the sink strength, large will be chromium depletion and larger will be the contribution to the total current. For example, the defect sink strength of a random grain boundary is higher than that of a twin boundary [39]. Therefore, the contribution to the total anodic current density would be higher from

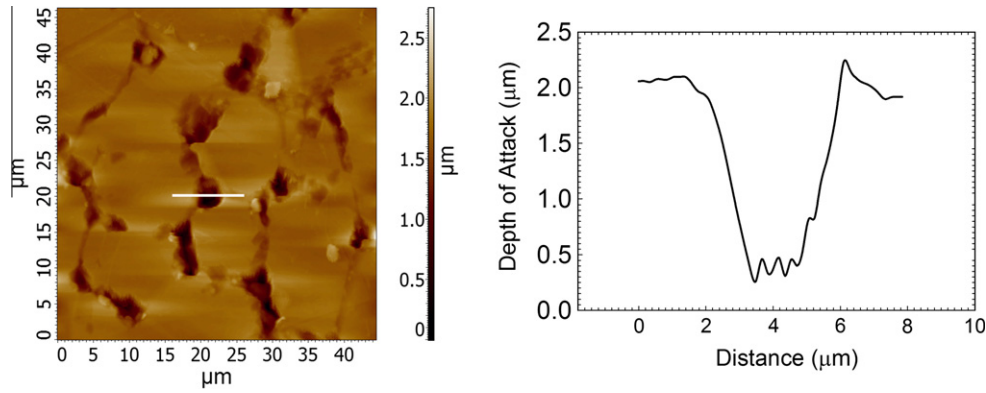


Fig. 7. An AFM micrograph for the sensitized (675 °C for 1 h) stainless steel after the DL-EPR test showing the depth of attack at grain boundary. The width and the depth of attack are 4 and 1.6 μm respectively.

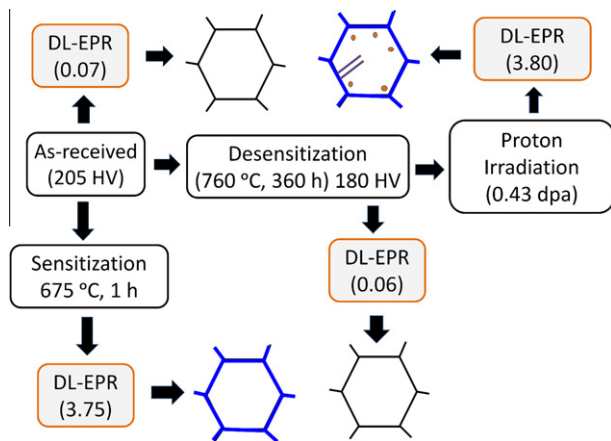


Fig. 8. Schematic representation of overall experimental and results, indicating attack, after the DL-EPR test, on grain boundaries, twin boundaries and pit-like features within grains at the depth of maximum attack. The sensitized specimen also showed severe attack on grain boundaries, however, attack on twin-boundaries and pit-like features were not noticed.

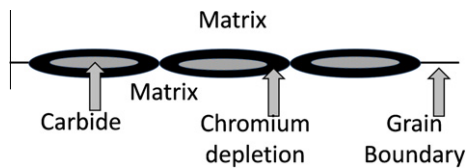


Fig. 9. Schematic representation of chromium depletion zones surrounding carbides at grain boundaries at carbide–matrix and carbide–carbide interfaces developed due to irradiation.

a random grain boundary than that from a twin boundary. The higher current from a given microstructural feature is also reflected by a higher depth of attack measured by AFM examination after the DL-EPR test. The depth of attack on grain boundaries and pit-like features were higher than that on twin boundaries as shown in Fig. 5. Therefore, the contribution to total anodic current density is higher for grain boundaries and pit-like features as compared to twin boundaries.

The contribution to total anodic current density would also be higher if the area fraction of a given microstructural feature is higher as compared to other microstructural features. For example, in grain boundary engineered (GBE) type 304 SS; the fraction of twin boundaries would be very high as compared to random

boundaries. In such cases the contribution of twin boundaries to the total anodic current will be higher than that from grain boundaries though the defect sink strength of a twin boundary is substantially lower than that of a random boundary. This was observed in the same material [41] after a suitable thermo-mechanical treatment used to produce a high fraction (0.54) of twin boundaries.

For the sensitized specimen, the DL-EPR value and the maximum current density during the reactivation loop were 3.89 and $735.5 \mu\text{A}/\text{cm}^2$, respectively, and the sensitized specimen did not show pit-like features and the attack on twin-boundaries. Thus, for the sensitized specimen, the contribution of the last two terms of the Eq. (3) to the total anodic current is nil. At the depth of 70 μm , for the desensitized specimen irradiated to 0.43 dpa the DL-EPR value and the maximum current density during the reactivation loop were 3.81 and $733.0 \mu\text{A}/\text{cm}^2$, respectively, and the irradiated desensitized specimen showed pit-like features and attack on twin-boundaries in addition to attack at grain boundaries. Thus, though the sensitized specimen and the irradiated desensitized SS show nearly equal DL-EPR values and reactivation current density, the current contribution (depth and the width of attack) was higher for the sensitized specimen at the grain boundaries as compared to that for the irradiated desensitized specimen. For the irradiated desensitized specimen, the current from pit-like features and twin boundaries also contributed to the total anodic current.

At the depth of 40 μm , for the desensitized specimen irradiated to 0.43 dpa, the DL-EPR value and the maximum current density during the reactivation loop of the DL-EPR test were 0.47 and $144 \mu\text{A}/\text{cm}^2$, respectively. At this depth, the number of pit-like features was less (Fig. 3b) as compared to that at the depth of 70 μm (Fig. 3c) where the maximum DL-EPR value was noticed. Thus, at the depth of 40 μm , the contribution of the last term in Eq. (3) to the total current is less than that from the first term; the term corresponds to grain boundary.

It may be noted that the current density during the reactivation loop is the measure of the metal dissolution at a particular microstructural feature. The higher current indicates higher metal dissolution and hence, higher depth of attack at a particular microstructural feature. Thus, lower current at the depth of 40 μm as compared to that at the depth of 70 μm indicates the lower depths of attack for microstructural features. This was confirmed by measurement of the depth of attack on different microstructural features by AFM as depicted in Fig. 5. Though, the irradiated desensitized SS (at the depth of maximum damage), shows wide attack at grain boundaries, the contribution to current due to this (term 1 in Eq. (3)) here is less as compared to thermally sensitized grain boundaries. This due to the fact that the wide at-

tack is because of dislodgement of carbides after the surrounding chromium depletion at the carbides get attacked in the DL-EPR test (Fig. 9).

4.5. Reproducibility of results

A combination of an electrochemical technique (DL-EPR) followed by AFM examination (to measure the depth of attack on various microstructural features) was used to characterize the extent of RIS in the irradiated desensitized type 304 SS. Though, EPR was used in the past to characterize RIS in austenitic SS, a combination of EPR and AFM examination was only recently used [40,41] to characterize the extent of RIS in austenitic SS. The advantage of the EPR technique over analytical techniques (such as STEM-EDS and AES) is that the DL-EPR value obtained on irradiated sample is a measure of chromium depletion on a large number of microstructural features like grain boundaries, pit-like features, and twin boundaries. On the other hand, analytical techniques reveal the extent of chromium depletion at individual grain boundaries. It may also be noted that extent of chromium depletion on a given grain boundary is a function of initial chromium level and grain boundary energy. Therefore, it is expected that for a given irradiation parameters (dose, dose rate, and temperature), the extent of chromium depletion will be different at different grain boundaries. In view of this, the measurements of chromium depletion at individual grain boundaries by analytical techniques may not be a true representation of the effect of a given set of irradiation parameters. On the other hand, in the case of electrochemical techniques, the results are obtained from a large number of grain boundaries hence the difference in chromium depletion due to grain boundary nature will be averaged out. This increases the reproducibility of the results obtained using the electrochemical techniques as compared to the results obtained using analytical techniques.

The proton-irradiation of energy 4.8 MeV results in uniform damage over first 70 μm of the depth (Fig. 2) and peak-damage region spans over approximately 10 μm . This provides opportunity for several measurements (7–10 measurements) in the uniform-damage region and 1–3 measurements in the peak-damage region using the electrochemical technique and AFM characterization approach. Most of the DL-EPR values in the uniform damage region were in the close range and the calculated level of dpa in the uniform damage region is almost constant. This implies that the results obtained using the DL-EPR technique is fairly reproducible. Similar observations were made for the same dose level of 0.43 dpa on the same material *without* desensitization [40] and on type 347 SS [41]. This further confirms the reproducibility of the results obtained using a combination of EPR and AFM examination.

4.6. Implications for resistance to RIS

Unlike thermally-sensitized SS, no chromium depletion zones are present in un-irradiated desensitized material. Therefore in the desensitized material during irradiation, the diffusion of Cr from the grain matrix (due to concentration gradient) to chromium depletion zones adjacent to grain boundaries would be absent. Hence in the desensitized material, the level of Cr depletion would be only affected by RIS and not by the Cr diffusion due to the concentration gradient.

The effect of M_{23}C_6 on RIS in austenitic stainless steels was not covered in previous studies [7–13] on the effect of thermal sensitization on RIS. In the present investigation, the effect of an indirect enrichment of Cr at grain boundaries in form of M_{23}C_6 on RIS (particularly Cr depletion) was investigated. The results obtained indicated that an indirect enrichment of Cr atoms at grain boundaries (due to M_{23}C_6) was not effective in reducing Cr depletion due to RIS

at grain boundaries. The results have also indicated that the location of formation of chromium depletion zones due to RIS has been shifted from grain boundaries (as would be in the case of type 304 SS without any M_{23}C_6 at grain boundaries) to regions adjacent to M_{23}C_6 . Extensive chromium depletion (as indicated by the DL-EPR value of as high as 3.81) adjacent to M_{23}C_6 indicated that the presence of M_{23}C_6 was not effective in controlling Cr depletion at grain boundaries due to RIS. Therefore, use of a desensitized SS would not offer any advantage against RIS in nuclear power plants.

5. Conclusions

Proton irradiation (to obtain irradiation damage equivalent to 0.43 dpa) was done at 300 °C on type 304 SS subjected to a desensitization heat treatment. The irradiated specimen was tested by the DL-EPR tests at various depths from the surface and characterization of the damage at various microstructural features was done by AFM. This was compared after DL-EPR and AFM characterization for the un-irradiated as-received, sensitized, and desensitized SS. The following are the main conclusions from the present investigation:

1. The attack during the DL-EPR test was noticed on various microstructural features viz. grain boundaries, twin boundaries, and pit-like features within grains. This indicates the development of chromium depletion regions at such microstructural features due to irradiation. This was in contrast to observation of attack only at grain boundaries for the un-irradiated as-received, sensitized and desensitized SS. The relative depth of attack after the DL-EPR can be represented in increasing order as twin-boundaries > pit-like features > grain boundaries.
2. The nature of RIS changed due to the presence of M_{23}C_6 at grain boundaries. The attack due to chromium depletion (during the DL-EPR test) started adjacent to grain boundaries (carbide–matrix interface) instead of at the grain boundaries. As irradiation progressed, the attack due to chromium depletion zones spread into grain boundaries (at the carbide–carbide interfaces).
3. The carbide–matrix and the carbide–carbide interface act as defects sinks for point defects leading to formation chromium depletion zones at these interfaces due to irradiation.
4. Though the EPR test does not cause attack at the M_{23}C_6 carbides at the grain boundaries, the attack due to formation of chromium depletion zones all around the carbide surfaces due to RIS led to removal (dislodgement) of M_{23}C_6 particles. Therefore, unlike for grain boundaries without any carbide, grain boundaries with M_{23}C_6 resulted in more depth and width of attack regions after the EPR test.
5. The width and depth of attack on grain boundaries in the un-irradiated thermally sensitized specimen was much more than that for the irradiated specimen.

References

- [1] Z. Jiao, J.T. Busby, G.S. Was, J. Nucl. Mater. 361 (2007) 218–227.
- [2] A. Etienne, M. Hernandez-Mayrol, C. Genevois, B. Radiguet, P. Parieige, J. Nucl. Mater. 400 (2010) 56–63.
- [3] P.L. Andresen, F.P. Ford, S.M. Murphy, J.M. Perks, in: Proceedings of 4th International Symposium on Environmental Degradation of Materials in Nuclear Power Systems – Water Reactors, NACE International, Houston, 1990.
- [4] M.J. Hackett, R. Najafabadi, G.S. Was, J. Nucl. Mater. 389 (2009) 279–287.
- [5] S.M. Bruemmer, J. Nucl. Mater. 216 (1994) 348.
- [6] S.M. Bruemmer, B.W. Arey, L.A. Charlot, Corrosion 48 (1992) 42.
- [7] K. Hide, T. Onchi, M. Mayuzumi, K. Dohi, Y. Futamura, Corrosion 51 (1995) 757.
- [8] T. Onchi, K. Hide, M. Mayuzumi, K. Dohi, T. Niho, Corrosion 53 (1997) 778.
- [9] K. Hide, T. Onchi, R. Oyamada, F.H. Kayano, J. Nucl. Mater. 232 (1996) 30.
- [10] T. Onchi, K. Hide, H.M. Chung, J. Nucl. Mater. 274 (1999) 341.
- [11] L.H. Wang, J. Kai, C.H. Tsai, C. Fong, J. Nucl. Mater. 258–263 (1998) 2046–2053.

- [12] O. Okada, K. Nakata, S. Kasahara, J. Nucl. Mater. 265 (1999) 232.
 [13] T.S. Duh, J.J. Kai, F.R. Chen, J. Nucl. Mater. 283–281 (2000) 198–204.
 [14] K. Kondou, A. Hasegawa, K. Abe, V. Kain, Y. Watanbe, in: Proceedings of 10th International Conference on Degradation of Materials in Nuclear Power Systems – Water Reactors, Paper No. 66, Nevada, American Nuclear Society and National Association of Corrosion Engineers, August 1991.
 [15] R. Katsura S. Nishimura, in: The NACE Annual Conference and Corrosion Show, Paper No. 91, CORROSION 92, 1992.
 [16] G.E.C. Bell, T. Inazumi, E.A. Kenik, T. Kondo, J. Nucl. Mater. 187 (1992) 170–179.
 [17] K. Kondou, A. Hasegawa, K. Abe, J. Nucl. Mater. 329–333 (2004) 652–656.
 [18] T. Inazumi, G.E.C. Bell, E.A. Kenik, K. Kiuchi, Corrosion 46 (1990) 786.
 [19] T. Inazumi, G.E. Bell, A. Hishinuma, Corrosion/90, National Association of Corrosion Engineers, Paper No. 507, 1990.
 [20] K.N. Adhe, V. Kain, S.S. Chouthai, H.S. Gadiyar, Indian J. Techcol. 28 (1990) 139–143.
 [21] J.F. Ziegler, J.P. Biersack, SRIM2003 Program, IBM Corp., Yorktown, NY, 2003.
 [22] M.J. Norgett, M.T. Robinson, I.M. Torrens, Nucl. Eng. Des. 33 (1975) 30.
 [23] A.P. Majidi, M.A. Steicher, Corrosion 40 (1984) 584–593.
 [24] C.Y. Chao, L.F. Lin, D.D. Macdonald, J. Electrochem. Soc. 128 (1991) 1187.
 [25] M. Urduidi-Macdonald, D.D. Macdonald, J. Electrochem. Soc. 134 (1987) 41.
 [26] V.V. Sagaradze, S.S. Lipin, M.A. Kirk, J. Nucl. Mater. 280 (2000) 345.
 [27] E.A. Kenik, K. Hojou, J. Nucl. Mater. 191–194 (1992) 1331.
 [28] Annual Book of Standard, ASTM A262-02, Practice A, Standard Practice for Detecting Standard Practices for Detecting Susceptibility to Intergranular Attack in Austenitic Stainless Steels, vol. 1.02, ASTM International, PA 19428-2959.
 [29] V. Kain, Yutaka Watanabe, J. Nucl. Mater. 302 (2002) 49.
 [30] V. Kain, R.C. Prasad, P.K. De, H.S. Gadiyar, ASTM J. Test. Eval. 23 (1995) 50–54.
 [31] V. Kain, S. Shinde, H. Gadiyar, ASM J. Mater. Eng. Perform. 36 (1994) 699–705.
 [32] V. Kain, R.C. Prasad, P.K. De, Corrosion 58 (2002) 15–38.
 [33] V. Kain, P.K. De, Int. J. Nucl. Energy Sci. Technol. 1 (2005) 220–231.
 [34] R.K. Dayal, N. Parvathavarthini, Baldev Raj, Int Mater Rev 50 (2005) 129–155.
 [35] D.A. Porter, K.E. Easterling, Phase Transformation in Metals and Alloys, second ed., Chapman & Hall Company, London, pp. 150–160.
 [36] S.M. Bruemmer, E.P. Simonen, P.M. Scott, P.L. Andresen, G.S. Was, J.I. Nelson, J. Nucl. Mater. 274 (1999) 299–314.
 [37] G.S. Was, Fundamentals of Radiation Materials Science, first ed., Springer-Verlag, 2007, pp. 236–242.
 [38] Y. Watanabe, V. Kain, T. Tonozuka, T. Shoji, T. Kondo, F. Masuyama, Scripta Mater. 42 (2000) 307–331.
 [39] P. Ahmedabadi, V. Kain, K. Arora, I. Samajdar, S.C. Sharma, S. Ravindra, P. Bhagwat, Unpublished results, Mater. Sci. Eng. A (2011), doi:10.1016/j.msea.2011.06.066.
 [40] P. Ahmedabadi, V. Kain, K. Arora, I. Samajdar, Corros. Sci. 53 (2011) 1465–1475.
 [41] P. Ahmedabadi, V. Kain, M. Gupta, I. Samajdar, S.C. Sharma, P. Bhagwat, R. Chowdhury, J. Nucl. Mater. doi:10.1016/j.jnucmat.2011.05.051.



Mr. Kabira Arora is graduated in Metallurgical Engineering (2010) from PEC University of Technology, Chandigarh, India. He is presently working in Mckinsey & Co. as a metallurgical consultant.



Prof. I. Samjadar is a metallurgical engineer working as a professor in Department of Metallurgical Engineering and Materials Science since 1998. He has graduated from Jadavpur University, Calcutta in 1987, post-graduated from University of Texas at El Paso, EL Paso, USA in 1991 and obtained his doctoral degree from Drexel University, Philadelphia, USA in 1994. His research interests include Crystallographic Texture, Microstructural Engineering and Thermomechanical Processing.



Mr. S.C. Sharma is working with Nuclear Physics Division, Bhabha Atomic Research Centre, Mumbai India and he has over 15 years of research experience in the field of Nuclear Physics. He has obtained his Master of Science in the field of Physics. His research interests include D.C Accelerator Instrumentation, Negative Ion Source development, Ultra High Vacuum Technology and Instrumentation and Irradiation setup for Nuclear, Environmental and Material science studies.



Mr. P. Bhagwat is working with Nuclear Physics Division, Bhabha Atomic Research Centre, Mumbai India and he has over 29 years of research experience in the field of Nuclear Physics. He has graduated in Electrical Engineering and his research interests include Design of Accelerator system, Application of accelerators and development of Radio frequency quadruple and ECR ion source.



Mr. Parag Ahmedabadi is a scientific officer in the Materials Science Division of Bhabha Atomic Research Centre, Mumbai, India. He has over 13 years of experience in the field Corrosion Science and Engineering and materials science. He obtained the graduate degree from M.S. University of Baroda in Metallurgical Engineering (1994) and the post-graduate degree from the Indian Institute of Technology in Process Metallurgy (1997). His fields of interests include electrochemical evaluation of proton-irradiated austenitic stainless steels, localized corrosion in stainless steels and nickel based alloys and failure analysis.



Dr. V. Kain is a metallurgical engineer working with Bhabha Atomic Research Centre, Mumbai. He has over 25 years of experience in the fields of materials science and corrosion science and technology. He obtained the doctoral degree from the Indian Institute of Technology Bombay in 1997. He has worked extensively on stainless steels, nickel based alloys, steels and Zirconium based alloys for nuclear power and allied industries. He has published 174 technical papers in reputed journals and conference proceedings. He is recipient of a number of awards from the department of atomic energy, Indian nuclear society, NACE International – India section and the scientific research council. He is a professor at the Homi Bhabha National Institute and guides students for master and doctoral degrees.